

# Highly multiplexed imaging of tumor tissues with subcellular resolution by mass cytometry

Charlotte Giesen<sup>1,8</sup>, Hao A O Wang<sup>2,3,8</sup>, Denis Schapiro<sup>1,4</sup>, Nevena Zivanovic<sup>1,5</sup>, Andrea Jacobs<sup>1</sup>, Bodo Hattendorf<sup>2</sup>, Peter J Schöffler<sup>6</sup>, Daniel Grolimund<sup>3</sup>, Joachim M Buhmann<sup>6</sup>, Simone Brandt<sup>7</sup>, Zsuzsanna Varga<sup>7</sup>, Peter J Wild<sup>7</sup>, Detlef Günther<sup>2</sup> & Bernd Bodenmiller<sup>1</sup>

Mass cytometry enables high-dimensional, single-cell analysis of cell type and state. In mass cytometry, rare earth metals are used as reporters on antibodies. Analysis of metal abundances using the mass cytometer allows determination of marker expression in individual cells. Mass cytometry has previously been applied only to cell suspensions. To gain spatial information, we have coupled immunohistochemical and immunocytochemical methods with high-resolution laser ablation to CyTOF mass cytometry. This approach enables the simultaneous imaging of 32 proteins and protein modifications at subcellular resolution; with the availability of additional isotopes, measurement of over 100 markers will be possible. We applied imaging mass cytometry to human breast cancer samples, allowing delineation of cell subpopulations and cell-cell interactions and highlighting tumor heterogeneity. Imaging mass cytometry complements existing imaging approaches. It will enable basic studies of tissue heterogeneity and function and support the transition of medicine toward individualized molecularly targeted diagnosis and therapies.

Tissues are complicated assemblies of multiple interacting cell types that communicate with each other to achieve physiological states. Many tools used to study tissues are based on imaging<sup>1</sup>. Fluorescent dyes coupled to affinity binders such as antibodies are common reporters, typically visualized by immunofluorescence microscopy (IFM)<sup>2</sup>. IFM enables analysis of most proteins and protein modifications down to nanometer resolution<sup>3</sup>. Genetically encoded fluorescent reporters, such as GFP, can also be analyzed in live cells<sup>4</sup>. When bound to DNA probes, RNA and DNA sequences can be imaged through FISH<sup>5</sup>. There are challenges common to all fluorescence-based approaches: sample autofluorescence affects the detection and quantitation of markers<sup>6</sup>. Furthermore, broad absorption and emission spectra practically limit the dynamic range and the number of molecules that can be simultaneously imaged to 7 (ref. 7). Multiplexing strategies

that rely on cycles of antibody staining, imaging, and fluorophore bleaching or antibody removal partially address this challenge<sup>8–10</sup>, but cycles can be incomplete, can change the antigenicity of the target specimen and are time consuming<sup>8–10</sup>.

Other imaging techniques to study tissues are used in life science research. Electron microscopy alone or coupled with fluorescence imaging allows analysis of cell morphological features and markers at picometer resolution<sup>11,12</sup>, but this is limited to a few markers. Matrix-assisted laser desorption/ionization (MALDI) imaging can visualize thousands of analytes—including proteins, lipids, metabolites and drugs—in an untargeted manner, typically with a resolution between 5 and 200  $\mu\text{m}$  but as low as 1  $\mu\text{m}$  (refs. 13–15). Whereas photocleavable mass tags bound to antibodies can be analyzed by MALDI imaging, multiplexing is currently limited by a lack of mass tags<sup>16</sup>. Metal distributions in tissues have been imaged by secondary-ion mass spectrometry (SIMS) at a resolution of 50 nm (refs. 17–19), but currently only seven isotopes can be imaged simultaneously by the dynamic SIMS required for trace-element analysis; and matrix effects, instrument costs and sampling under vacuum prevent routine applications<sup>17,18</sup>. Metal distributions in tissues at a spatial resolution of 5–200  $\mu\text{m}$  can be visualized at atmospheric pressure by laser ablation coupled to inductively coupled plasma mass spectrometry (LA-ICP-MS)<sup>17,19,20</sup>. The spatial resolution of LA-ICP-MS is limited by only the laser spot size and analyte detection limit<sup>17,20</sup>, and it has been applied in two- and three-parameter immunohistochemistry (IHC) approaches<sup>21,22</sup>. For higher-multiplexed applications at subcellular resolution, the simultaneous isotope detection, analysis speed and sensitivity must be improved.

Mass cytometry uses a time-of-flight ICP-MS instrument (CyTOF system (Fluidigm, formerly DVS Sciences)) that can detect dozens of markers simultaneously at a high mass-spectrum acquisition frequency on the timescale of high-frequency laser ablation<sup>23</sup>. It measures the abundance of metal isotopes tagged to

<sup>1</sup>Institute of Molecular Life Sciences, University of Zürich, Zürich, Switzerland. <sup>2</sup>Department of Chemistry, Swiss Federal Institute of Technology Zürich, Zürich, Switzerland. <sup>3</sup>Swiss Light Source, Paul Scherrer Institute, Villigen, Switzerland. <sup>4</sup>Systems Biology Ph.D. Program, Life Science Zürich Graduate School, ETH Zürich and University of Zürich, Zürich, Switzerland. <sup>5</sup>Molecular Life Science Ph.D. Program, Life Science Zürich Graduate School, ETH Zürich and University of Zürich, Zürich, Switzerland. <sup>6</sup>Department of Computer Science, Swiss Federal Institute of Technology Zürich, Zürich, Switzerland. <sup>7</sup>Institute of Surgical Pathology, University Hospital Zürich, Zürich, Switzerland. <sup>8</sup>These authors contributed equally to this work. Correspondence should be addressed to B.B. ([bernd.bodenmiller@imls.uzh.ch](mailto:bernd.bodenmiller@imls.uzh.ch)) or D. Günther ([guenther@inorg.chem.ethz.ch](mailto:guenther@inorg.chem.ethz.ch)).

antibodies, and amplification is achieved by a polymeric metal-chelating reagent or metal nanoparticles<sup>23,24</sup>. Because of these features, mass cytometry could be adapted to meet the sensitivity and multiplexing needs for tissue analysis at subcellular resolution<sup>23</sup>. Previously, mass cytometry has been used only to analyze cells in suspension, and information on cell-cell interactions within tissue or tumor microenvironments has therefore been lost<sup>25–30</sup>. Here we describe imaging mass cytometry—an approach that combines CyTOF mass cytometry with immunocytochemistry (ICC) and IHC techniques, a high-resolution laser ablation system and a low-dispersion laser ablation chamber—to image 32 proteins and their modifications simultaneously at a cellular resolution of 1  $\mu\text{m}$  (ref. 31).

Applying this approach, we analyzed human formalin-fixed, paraffin-embedded (FFPE) breast cancer samples and human mammary epithelial (HMLE) cells<sup>32</sup>. Analysis across cell states revealed substantial tumor microenvironment heterogeneity. Imaging mass cytometry can be combined with other imaging techniques and has the potential to influence both biological research and clinical management.

## RESULTS

### Imaging mass cytometry

We introduce here an imaging technique that extends the multiplexed analysis capabilities of CyTOF-based mass cytometry<sup>23,27,30</sup> to make spatially resolved measurements. We developed a workflow to couple mass cytometry, ICC and IHC analyses with a high-resolution laser ablation system to allow analysis of adherent cells and tissue sections with cellular resolution of 1  $\mu\text{m}$  (Fig. 1). In the first step, the cell sample or tissue section

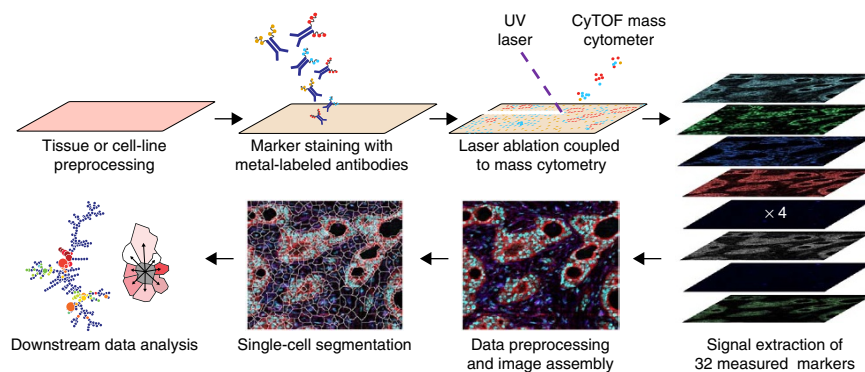


**Figure 1** | Workflow of imaging mass cytometry.

was prepared for antibody labeling using routine ICC and IHC protocols (Online Methods). Antibodies were selected to target proteins and protein modifications relevant to breast cancer. Before staining, antibodies were tagged with a unique rare-earth-metal isotope of defined atomic mass. Currently, 32 rare-earth-metal isotopes are available as reporters. After air drying, the sample was positioned in a laser ablation chamber recently developed to minimize aerosol dispersion for high-resolution, high-throughput and highly sensitive analyses<sup>31</sup>. The tissue was then ablated spot by spot and line by line, and the ablated material was then transported by a mixed argon and helium stream to the CyTOF mass cytometer.

As determined from the data sets presented in this study, the signals of individual laser shots at 20 Hz were fully separated (Supplementary Fig. 1), and the limit of detection was approximately six ion counts (corresponding to ~500 molecules), assuming Poisson statistics (Online Methods). After data preprocessing, the 32 transient, single isotope signals were plotted using the coordinates of each single laser shot, and a high-dimensional image of the sample was generated by overlaying all analyzed measurement channels. Next, single-cell features were computationally segmented using a watershed algorithm, and the single-cell marker expression data were extracted (Online Methods). These single-cell data were used for all downstream data analyses and to investigate cell subpopulations within a set of 21 tumor and normal samples in total from 20 breast cancer patients.

### Validity of the approach

To evaluate the validity of imaging mass cytometry for IHC, we first performed experiments using FFPE breast cancer samples to ensure that metal labeling of the antibodies did not interfere with their target specificity. We compared unlabeled and metal-labeled antibodies using IFM analysis on serial sections of tissues no. 210 and no. 37, which are from tumors of the same type (Fig. 2a and Supplementary Fig. 2). We observed no apparent change in antibody specificity due to the metal labeling. Quantitative

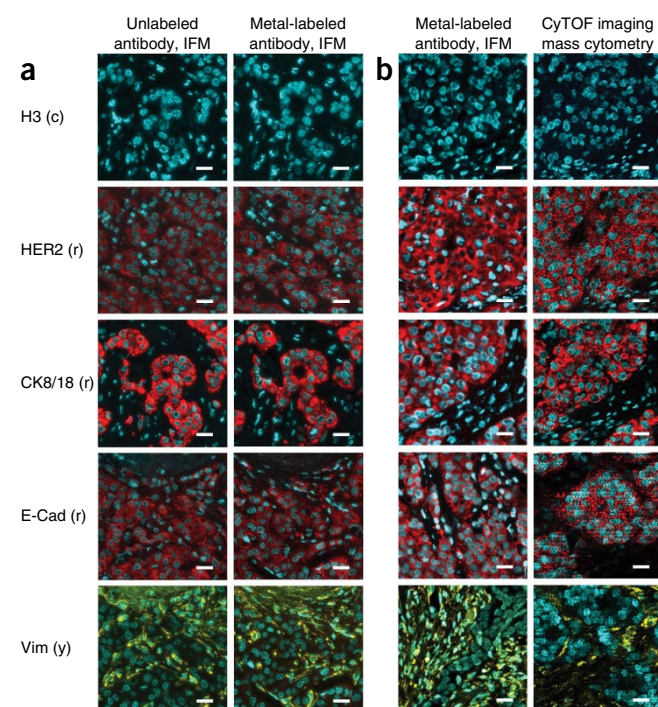
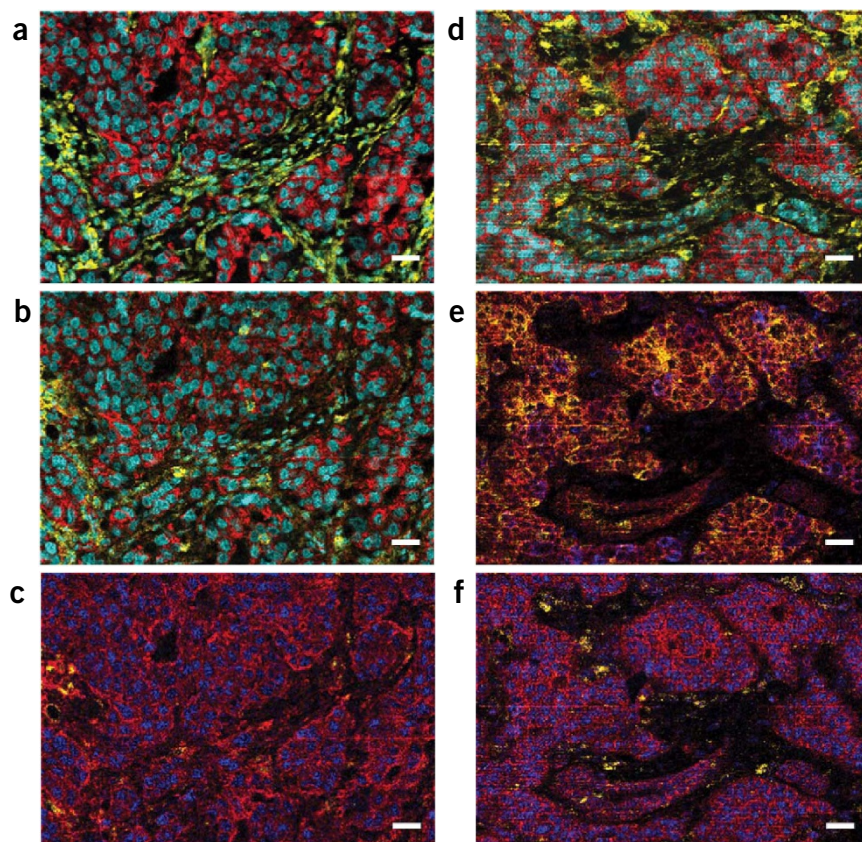


**Figure 2** | Validation of imaging mass cytometry. (a) IFM on serial breast cancer tissue sections of the luminal HER2<sup>+</sup> subtype (case no. 37) using unlabeled and metal-labeled antibodies recognizing the indicated markers. (b) IFM and CyTOF imaging mass cytometry on breast cancer tissue sections of the luminal HER2<sup>+</sup> subtype (case nos. 210, 23 and 37) using metal-labeled antibodies recognizing the indicated markers. E-cadherin (E-Cad) and vimentin (Vim) were not analyzed on serial sections. Both Hoechst 33258 in IFM images and H3 in all images are shown in cyan (c). r, red; y, yellow; CK8/18, cytokeratin 8/18. Scale bars, 25  $\mu\text{m}$ .



**Figure 3** | Representative mass cytometry images of luminal HER2<sup>+</sup> breast cancer tissue samples. Case nos. 210 (a–c) and 23 (d–f) are shown. For both tissues, a total of 32 proteins and phosphorylation sites were measured simultaneously at 1- $\mu$ m resolution (**Supplementary Tables 1 and 2**). (a) Overlay of cytokeratin 8/18 (red), H3 (cyan) and vimentin (yellow). (b) Overlay of cytokeratin 7 (red), H3 (cyan) and CD44 (yellow). (c) Overlay of pan-actin (red), progesterone receptor (blue) and CD68 (yellow). (d) Overlay of HER2 (red), H3 (cyan) and vimentin (yellow). (e) Overlay of E-cadherin (red), cytokeratin 7 (yellow) and phosphorylation on S235/S236 on S6 (blue). (f) Overlay of  $\beta$ -catenin (red), estrogen receptor (blue) and CD68 (yellow). Scale bars, 25  $\mu$ m. For each unique tissue section, the measurement was performed once due to the destructive nature of imaging mass cytometry. 23 tissues sections in total were imaged for this manuscript.



analysis showed that the differences of the mean single-cell fluorescence intensity of each marker between unlabeled and metal-labeled antibodies, although significant, were small: -7% for histone H3 (H3;  $P < 4.7 \times 10^{-8}$ ), 7% for epidermal growth factor receptor 2 (HER2;  $P < 1.0 \times 10^{-12}$ ), 27% for cytokeratin 8/18 ( $P < 3.7 \times 10^{-3}$ ), 7% for E-cadherin ( $P < 2.5 \times 10^{-11}$ ), -2% for vimentin ( $P < 4.2 \times 10^{-2}$ ) and 22% for cytokeratin 7 ( $P < 5.8 \times 10^{-36}$ ) (**Supplementary Fig. 3**). These differences are well within the range of the variability typically observed in experimental procedures and among serial tissue sections that are similar but not identical. The similarity between unlabeled and metal-labeled antibodies was further confirmed by the congruency of the single-cell marker fluorescence intensity distributions over the analyzed intensity range for all tested antibody pairs<sup>23,27,30</sup> (**Supplementary Fig. 3**).

We then investigated whether images generated by mass cytometry reproduced the staining patterns and the percentage of cells expressing a given marker as determined by IFM. We used IFM and imaging mass cytometry on tumor sections (no. 210 and no. 23) from the same luminal HER2<sup>+</sup> subtype each; both methods

gave antibody staining patterns expected for this subtype (**Fig. 2b**, **Supplementary Fig. 4** and **Supplementary Tables 1 and 2**). Markers we typically observed in the nuclei were H3, which is a nucleosomal DNA packaging protein (**Fig. 2b**), and progesterone receptor (PR), a transcription factor activated in luminal breast cancer (**Supplementary Fig. 4**). We typically observed HER2, an epidermal growth factor receptor family member, as well as cytokeratin 8/18 and the epithelial cell-cell junction component E-cadherin, in the plasma membrane. The presence of vimentin indicated the stromal compartment. These patterns are in agreement with antibody validation by others (**Supplementary Note 1**). The percentages of tumor cells expressing the analyzed markers were similar in IFM and imaging mass cytometry on serial tissue sections (**Fig. 2b**): 100% and 100% for H3, respectively; 75% and 79% for HER2; and 63% and 66% for cytokeratin 8/18. Full-size mass cytometry images of further markers are shown (**Fig. 3** and **Supplementary Fig. 5**).

We also assessed whether single-plex IHC, duplex IFM and 32-plex imaging mass cytometry analysis yielded congruent results. Single-plex IHC analysis using identical antibodies (cytokeratin 8/18 and H3) or using different antibody clones but

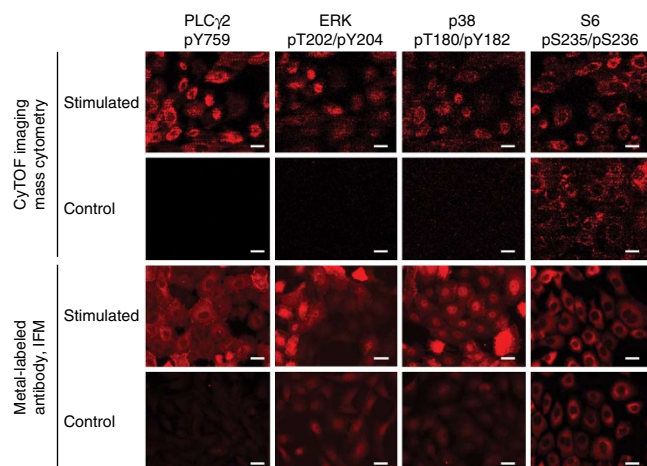
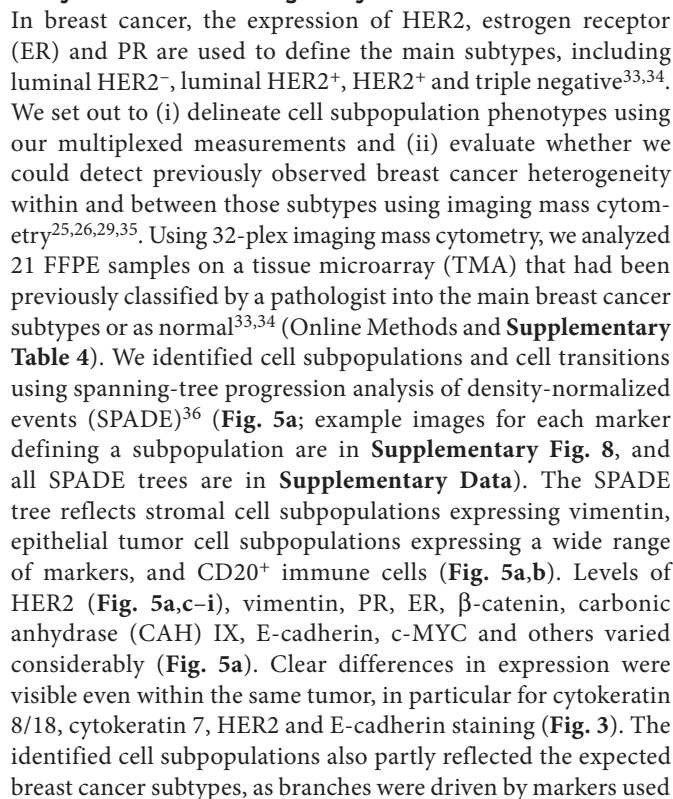


**Figure 4** | Analysis of adherent cells by IFM and imaging mass cytometry. The micrographs show human mammary epithelial cells labeled and imaged as indicated with antibodies recognizing a panel of phosphorylated residues, without ('control') and with ('stimulated') a 30-min treatment with the tyrosine phosphatase inhibitor vanadate. Scale bars, 25  $\mu$ m. Exposure was kept constant for each control-stimulated comparison but not between different antibodies. Note that primary- and secondary-antibody detection were used for imaging mass cytometry and IFM, respectively. The latter will increase the sensitivity of the detection.

These results show that imaging mass cytometry enables simultaneous and highly multiplexed tissue and adherent cell imaging with subcellular resolution. There were no apparent changes in specificity and performance between unlabeled and metal-labeled antibodies, nor between antibodies used in single-plex IHC, duplex IFM and multiplex analyses using imaging mass cytometry.





for patient classification: for example, HER2<sup>+</sup> and luminal HER2<sup>+</sup> (Fig. 5e,f,h,i and Supplementary Note 2).

Seven samples were classified as either HER2<sup>+</sup> or luminal HER2<sup>+</sup> (refs. 33,34). These samples populated the SPADE tree, but there were also unique subpopulations differing in cytokeratin 8/18, E-cadherin,  $\beta$ -catenin and c-MYC expression (Fig. 5a); see, for example, luminal HER2<sup>+</sup> tumor no. 210 (Fig. 5e), which overexpressed c-MYC (Supplementary Fig. 9). These differences within the same breast cancer subtype indicate interpatient tumor heterogeneity (Fig. 5e,f,h,i). Although patient classification by imaging mass cytometry largely agreed with the surgical pathologist's independent assessment, there were exceptions. For example, in one triple-negative case (no. 162), detectable levels of HER2 were expressed (Supplementary Fig. 10a), which could be subsequently confirmed by IHC (Supplementary Fig. 10b).

The samples differed in the expression of other markers as well, including CAH IX, a reporter of hypoxia. For two cases, a local tumor recurrence (no. 260) and a triple-negative case (no. 201), the SPADE analysis displayed cellular transitions (Fig. 5a and Supplementary Fig. 11a); CAH IX gradients were visible with the concentration increasing toward the tumor core<sup>37</sup> (Supplementary Fig. 11b,c). The SPADE tree also revealed stromal cells with high levels of phosphorylation of S235 and S236 on S6 (Fig. 5a). These cells were sometimes close to or at the boundary between tumor and stromal cells (Supplementary Fig. 12), a result indicating that signaling activity of stromal cells may be induced at the tumor boundary by other cell types<sup>26</sup>.

These data demonstrate that mass cytometry enables simultaneous imaging of cell-type markers, signaling activity and hallmarks of cancer, such as hypoxia. Taken together, these analyses delineated breast cancer cell subpopulations present in the analyzed FFPE samples, identified their spatial arrangement, and revealed differences within the same patient and among patients with the same tumor classification.

## DISCUSSION

Imaging mass cytometry exploits the multiparameter capabilities of the CyTOF mass cytometer for the simultaneous, rapid and spatially resolved analysis of 32 proteins and their modifications with subcellular resolution. Here we showed the validity of the technology and then analyzed adherent cells and breast cancer and normal breast tissue from 20 patients. Metal labeling of the antibodies did not destroy or apparently change antigen specificity. Multiplexed imaging mass cytometry also reproduced the staining patterns obtained with single-plex IHC and duplex IFM. Therefore, antibodies validated for IHC will likely be applicable for imaging mass cytometry.

A number of characteristics make imaging mass cytometry highly quantitative: there is no sample autofluorescence, there are no matrix effects as found in MALDI and SIMS imaging<sup>15</sup>, there is no need for an amplification step such as is often applied in IHC, the tissue is completely sampled and the approach has a wide dynamic range of  $\sim 10^5$ . Appropriate standards will enable the absolute quantification of cellular markers and, therefore, determination of accurate thresholds to define a patient's state. Antibodies, however, continue to

pose a limitation: often antibodies are not available for a given target or in the format needed for mass cytometry, and those that work well in single-plex assays may behave differently in multiplex assays.

The sample preparation necessary for imaging mass cytometry is identical to that for ICC and IHC analyses: this will enable (i) fast implementation of imaging mass cytometry on the now broadly available CyTOF instruments; (ii) adaptation to imaging mass cytometry of existing assays to evaluate the genome, the transcriptome and other cellular parameters to increase the information gained from a tissue; and (iii) analysis of samples with other methods before imaging mass cytometry. Alternatively, serial tissue sections can be analyzed by imaging mass cytometry and by any other approach. MALDI imaging would be an ideal complementary approach, as MALDI monitors thousands of analytes in an untargeted and semistochastic manner<sup>13–15</sup>. The cell states defined by mass cytometry could then be registered with the MALDI imaging data to provide an 'omic systems-level analysis of samples.

At present, 32 rare-earth-metal isotopes are available for antibody labeling, but with the current system, over 100 markers can be detected simultaneously<sup>23</sup>. Increased isotope availability and novel metal-chelating chemistries will make such measurements possible soon. To measure an area of 0.5 mm  $\times$  0.5 mm at 1- $\mu$ m resolution takes  $\sim 3.5$  h. Novel laser ablation chamber designs under development are expected to provide for several-fold-higher scanning speeds and throughput. Reduction of aerosol dispersion, use of multiple antibody clones against a target, and an increase in the number of metal atoms bound to each antibody through the use of metal nanoparticles will substantially boost sensitivity. We expect that quantitative analysis on  $\sim 100$  markers on a given tissue with submicrometer resolution in less than 1 h will be possible in the future.

Our SPADE analysis highlights intra- and interpatient heterogeneity by delineating the subpopulations present in the breast cancer samples<sup>25,26,29</sup>. However, imaging mass cytometry yields information about only the tumor region imaged, and different cell subpopulations can exist in different regions of a tumor<sup>38</sup>. Multiple regions, such as the invasive front, center and periphery, must therefore be imaged. Furthermore, as imaging approaches provide only a single snapshot of tumor development, multiple images over time may be necessary to reveal relevant phenotypes. Owing to the detection limit of imaging mass cytometry, small abundance differences at the detection threshold can artificially increase the observed tumor heterogeneity; similar effects are caused by incorrect tissue cell segmentation (Supplementary Note 3). Finally, for tumor biology to be understood, the increase in data complexity should be accompanied by orthogonal data sets, novel algorithms, and experiments tailored to address a specific biological question.

Using the multiplexing capability of imaging mass cytometry will enable deep studies of tissue and tumor biology. We envision that spatial relationships of complex cell states that include several layers of 'omics information, cell-cell interactions and communication, transcellular networks and mathematical models of cellular assemblies might become new 'biomarkers' and paradigms in a systems biology approach to understand and diagnose disease and to guide treatment.

## METHODS

Methods and any associated references are available in the [online version of the paper](#).

Note: Any Supplementary Information and Source Data files are available in the [online version of the paper](#).

## ACKNOWLEDGMENTS

We thank M. Storz for preparing the histological slides and the TMA sections; S. Dettwiler, A. Bohnert, A. Fitsche; the entire Trace Element and Micro Analysis group at ETH Zürich for their experimental support and discussions; N. Daga and C. von Mering for their feedback on data analysis; the ETHZ LAC workshop for their support in design and construction of the laser ablation chamber; and the Lehner and Luschign groups for giving us access to their immunofluorescence microscopes. This work was supported by a Society in Science, The Branco Weiss Fellowship, administered by the ETH Zürich (C.G.); the Swiss National Science Foundation (SNSF) project grants 200021-119779 (H.A.O.W.), 200021-119779 (D. Günther), 31003A-143877 (D. Günther) and 31003A-143877 (B.B.); an ETH Zürich Pioneer Fellowship (H.A.O.W.); the SystemsX PhosphoNet-PPM grant (P.J.W. and B.B.); a Baugarten Foundation grant (SGGP) (P.J.W.); a EU VIGOR++ project FP7/2007-2013, #270379 (P.J.S. and J.M.B.); an SNSF R'Equip grant 316030-139220 (B.B.); an SNSF Assistant Professorship grant PP00P3-144874 (B.B.); a Swiss Cancer League grant (B.B.); and funding from the European Research Council (ERC) under the European Union's Seventh Framework Programme (FP7/2007-2013)/ERC Grant Agreement no. 336921 (B.B.).

## AUTHOR CONTRIBUTIONS

C.G., H.A.O.W., N.Z., A.J., D. Grolimund, Z.V., P.J.W., D. Günther and B.B. designed and performed experiments. H.A.O.W., D. Grolimund and B.B. established the tissue laser ablation system. C.G., H.A.O.W., D.S., N.Z., A.J., P.J.S. and D. Grolimund performed data analysis. S.B., Z.V. and P.J.W. assembled, provided and classified tumor samples. D.S., P.J.S. and J.M.B. arranged image analysis and single-cell segmentation. C.G., H.A.O.W., D.S., N.Z., P.J.W., D. Grolimund, D. Günther and B.B. prepared the figures and wrote the manuscript. D. Günther and B.B. conceived of and supervised the project. All authors reviewed and approved the manuscript.

## COMPETING FINANCIAL INTERESTS

The authors declare competing financial interests: details are available in the [online version of the paper](#).

Reprints and permissions information is available online at <http://www.nature.com/reprints/index.html>.

- Kherlopian, A.R. *et al.* A review of imaging techniques for systems biology. *BMC Syst. Biol.* **2**, 74 (2008).
- Lichtman, J.W. & Conchello, J.A. Fluorescence microscopy. *Nat. Methods* **2**, 910–919 (2005).
- Lubeck, E. & Cai, L. Single-cell systems biology by super-resolution imaging and combinatorial labeling. *Nat. Methods* **9**, 743–748 (2012).
- Giepmans, B.N., Adams, S.R., Ellisman, M.H. & Tsien, R.Y. The fluorescent toolbox for assessing protein location and function. *Science* **312**, 217–224 (2006).
- Langer-Safer, P.R., Levine, M. & Ward, D.C. Immunological method for mapping genes on *Drosophila* polytene chromosomes. *Proc. Natl. Acad. Sci. USA* **79**, 4381–4385 (1982).
- Robertson, D., Savage, K., Reis-Filho, J.S. & Isacke, C.M. Multiple immunofluorescence labelling of formalin-fixed paraffin-embedded (FFPE) tissue. *BMC Cell Biol.* **9**, 13 (2008).
- Tsurui, H. *et al.* Seven-color fluorescence imaging of tissue samples based on Fourier spectroscopy and singular value decomposition. *J. Histochem. Cytochem.* **48**, 653–662 (2000).
- Gerdes, M.J. *et al.* Highly multiplexed single-cell analysis of formalin-fixed, paraffin-embedded cancer tissue. *Proc. Natl. Acad. Sci. USA* **110**, 11982–11987 (2013).
- Schubert, W. *et al.* Analyzing proteome topology and function by automated multidimensional fluorescence microscopy. *Nat. Biotechnol.* **24**, 1270–1278 (2006).
- Wählby, C., Erlandsson, F., Bengtsson, E. & Zetterberg, A. Sequential immunofluorescence staining and image analysis for detection of large numbers of antigens in individual cell nuclei. *Cytometry* **47**, 32–41 (2002).
- Martell, J.D. *et al.* Engineered ascorbate peroxidase as a genetically encoded reporter for electron microscopy. *Nat. Biotechnol.* **30**, 1143–1148 (2012).
- Giepmans, B.N., Deerinck, T.J., Smarr, B.L., Jones, Y.Z. & Ellisman, M.H. Correlated light and electron microscopic imaging of multiple endogenous proteins using Quantum dots. *Nat. Methods* **2**, 743–749 (2005).
- Cornett, D.S., Reyzer, M.L., Chaurand, P. & Caprioli, R.M. MALDI imaging mass spectrometry: molecular snapshots of biochemical systems. *Nat. Methods* **4**, 828–833 (2007).
- Schober, Y., Guenther, S., Spengler, B. & Römpf, A. Single cell matrix-assisted laser desorption/ionization mass spectrometry imaging. *Anal. Chem.* **84**, 6293–6297 (2012).
- McDonnell, L.A. & Heeren, R.M. Imaging mass spectrometry. *Mass Spectrom. Rev.* **26**, 606–643 (2007).
- Thiery, G. *et al.* Multiplex target protein imaging in tissue sections by mass spectrometry—TAMSIM. *Rapid Commun. Mass Spectrom.* **21**, 823–829 (2007).
- Qin, Z., Caruso, J.A., Lai, B., Matusch, A. & Becker, J.S. Trace metal imaging with high spatial resolution: applications in biomedicine. *Metallomics* **3**, 28–37 (2011).
- Zhang, D.S. *et al.* Multi-isotope imaging mass spectrometry reveals slow protein turnover in hair-cell stereocilia. *Nature* **481**, 520–524 (2012).
- Becker, J.S. *et al.* Bioimaging of metals and biomolecules in mouse heart by laser ablation inductively coupled plasma mass spectrometry and secondary ion mass spectrometry. *Anal. Chem.* **82**, 9528–9533 (2010).
- Koch, J. & Günther, D. Review of the state-of-the-art of laser ablation inductively coupled plasma mass spectrometry. *Appl. Spectrosc.* **65**, 155–162 (2011).
- Seuma, J. *et al.* Combination of immunohistochemistry and laser ablation ICP mass spectrometry for imaging of cancer biomarkers. *Proteomics* **8**, 3775–3784 (2008).
- Giesen, C. *et al.* Multiplexed immunohistochemical detection of tumor markers in breast cancer tissue using laser ablation inductively coupled plasma mass spectrometry. *Anal. Chem.* **83**, 8177–8183 (2011).
- Bandura, D.R. *et al.* Mass cytometry: technique for real time single cell multitarget immunoassay based on inductively coupled plasma time-of-flight mass spectrometry. *Anal. Chem.* **81**, 6813–6822 (2009).
- Lou, X. *et al.* Polymer-based elemental tags for sensitive bioassays. *Angew. Chem. Int. Ed. Engl.* **46**, 6111–6114 (2007).
- Marusyk, A., Almendro, V. & Polyak, K. Intra-tumour heterogeneity: a looking glass for cancer? *Nat. Rev. Cancer* **12**, 323–334 (2012).
- Hanahan, D. & Coussens, L.M. Accessories to the crime: functions of cells recruited to the tumor microenvironment. *Cancer Cell* **21**, 309–322 (2012).
- Bendall, S.C. *et al.* Single-cell mass cytometry of differential immune and drug responses across a human hematopoietic continuum. *Science* **332**, 687–696 (2011).
- Psaila, B. & Lyden, D. The metastatic niche: adapting the foreign soil. *Nat. Rev. Cancer* **9**, 285–293 (2009).
- Hanahan, D. & Weinberg, R.A. Hallmarks of cancer: the next generation. *Cell* **144**, 646–674 (2011).
- Bodenmiller, B. *et al.* Multiplexed mass cytometry profiling of cellular states perturbed by small-molecule regulators. *Nat. Biotechnol.* **30**, 858–867 (2012).
- Wang, H.A.O. *et al.* Fast chemical imaging at high spatial resolution by laser ablation inductively coupled plasma mass spectrometry. *Anal. Chem.* **85**, 10107–10116 (2013).
- Elenbaas, B. *et al.* Human breast cancer cells generated by oncogenic transformation of primary mammary epithelial cells. *Genes Dev.* **15**, 50–65 (2001).
- Perou, C.M. *et al.* Molecular portraits of human breast tumours. *Nature* **406**, 747–752 (2000).
- Sims, A.H., Howell, A., Howell, S.J. & Clarke, R.B. Origins of breast cancer subtypes and therapeutic implications. *Nat. Clin. Pract. Oncol.* **4**, 516–525 (2007).
- Nowell, P.C. The clonal evolution of tumor cell populations. *Science* **194**, 23–28 (1976).
- Qiu, P. *et al.* Extracting a cellular hierarchy from high-dimensional cytometry data with SPADE. *Nat. Biotechnol.* **29**, 886–891 (2011).
- Lock, F.E. *et al.* Targeting carbonic anhydrase IX depletes breast cancer stem cells within the hypoxic niche. *Oncogene* **32**, 5210–5219 (2013).
- Davila, E. & Amazon, K. The clinical importance of the heterogeneity of HER2 neu. *Case Rep. Oncol.* **3**, 268–271 (2010).

## ONLINE METHODS

**Data and software availability.** All raw data, image source data, cell segmentation masks, algorithms and software (**Supplementary Software**) for data processing and SPADE trees (**Supplementary Data**) are available at <http://www.cytobank.org/bodenmillerlab/>.

**Patients and specimen characteristics.** TMAs contained FFPE breast cancer tissues of the major subtypes and normal breast tissues, and were previously described<sup>39</sup>. For this study, all tumors analyzed by imaging mass cytometry were reevaluated by two experienced clinical pathologists (J.P. Theurillat and Z.V.) by H&E to identify representative areas. Tumor stage and Bloom-Richardson-Elston (BRE) grade were assigned according to the Union for International Cancer Control (UICC) and World Health Organization (WHO) criteria. Classification of breast cancer subtypes was based on IHC expression patterns of ER, PR and HER2. HER2 status was assessed by HER2 IHC and HER2 FISH<sup>1</sup> (**Supplementary Table 4**). The study was approved by the ethical committee of the Canton Zurich (KEK-ZH-no.: 2012-0553). According to the Swiss Federal Law for research, a positive vote of an ethical committee in a retrospective study is sufficient for using tissue for research purposes without further need of individual informed consents for the samples.

**Antibodies.** Metal-labeled antibodies were prepared according to the Fluidigm (formerly DVS Sciences) protocol. Antibodies were obtained in carrier/protein-free buffer and then prepared using the MaxPar antibody conjugation kit (Fluidigm (formerly DVS Sciences))<sup>24</sup>. After we determined the percent yield by measurement of absorbance at 280 nm, the metal-labeled antibodies were diluted in Candor PBS Antibody Stabilization solution (Candor Bioscience) for long-term storage at 4 °C. Antibodies used in this study are listed in **Supplementary Tables 1–3, 5 and 6**.

**Preparation of HMLE cells for imaging mass cytometry.** HMLE cells were obtained from the Weinberg lab (Whitehead Institute for Biomedical research) and tested for mycoplasma contamination. Cells were cultured in HuMEC Ready Medium (Gibco) at 37 °C with 5% CO<sub>2</sub> as described<sup>32</sup>. For IFM imaging, cells were grown to ~80% confluency on glass coverslips and were either mock treated or treated with 125 μM vanadate for 30 min at 37 °C. Cells were prepared for imaging mass cytometry and IFM using a standard ICC protocol<sup>40</sup>. The antibodies are listed in **Supplementary Table 3**.

**Preparation of breast cancer tissue sections for IHC, IFM and imaging mass cytometry analyses.** All classical IHC stains of the TMA used in this study were conducted on a Ventana Benchmark XT using Ventana prediluted antibodies, and standard protocols (cc1m for HER2, clone 3B5; cc1 standard for PR, clone 1E2). The stainings for anti-cytokeratin 8/18 and anti-H3 (**Supplementary Fig. 6**) were performed manually: the tissue section was de-waxed overnight in xylene and rehydrated in a graded series of alcohol (ethanol absolute, ethanol:deionized water 90:10, 80:20, 70:30, 50:50, 0:100; 10 min each<sup>6</sup>). Heat-induced epitope retrieval was conducted in a water bath at 92–94 °C in Tris-EDTA buffer at pH 9 for 20 min. After immediate cooling, the TMA was blocked with 3% BSA in TBS for 45 min. TMA samples were incubated

overnight at 4 °C with a final concentration of 7.5 μg/mL of primary antibody (diluted in TBS/0.1% Triton X-100/1% BSWA). Samples were then washed with 2× TBS/0.1% Triton X-100 and 2× TBS. The secondary-antibody staining for cytokeratin 8/18 and H3 was performed with the EnVision Detection Systems Peroxidase/DAB, Rabbit/Mouse Kit (Dako) following the manufacturer's protocol. For immunofluorescence (**Fig. 2** and **Supplementary Figs. 2–4**), secondary antibodies Alexa Fluor 647 goat anti-mouse and Alexa Fluor 488 goat anti-rabbit were used at a final concentration of 2 μg/mL for a 1-h incubation at room temperature. After a wash with 2× TBS/0.1% Triton X-100 and 2× TBS, a 3-min staining with Hoechst 33258 (2 μg/mL in PBS) was performed. After a final wash step with 2× TBS/0.1% Triton X-100 and 2× TBS, IFM was performed. Samples were imaged with a Zeiss Axio Observer.Z1 (camera, AxioCam MRm; objective, Ec Plan-Neofluar 40× / 0.75 Ph2; filter sets, 02 (DAPI), 38 (Alexa Fluor 488) and 50 (Alexa Fluor 647)). Images were acquired using AxioVision software (AxioVision Rel 4.8), and the acquisition was performed on the same day to prevent differences due to emission changes of the light sources. In addition, exposure times for a given marker were kept constant for the comparative analysis of each antibody. Images were processed using ImageJ software (ImageJ 1.440). Serial samples were imaged with a Zeiss Mirax Midi Slide Scanner (camera, AxioCam monochrome CCD; objective, 20× (dry, NA = 0.8); filter, DAPI, eGFT, mPlum and Cy5). Images were acquired using Mirax Scan 1.12.

Tissue no. 23 and FFPE breast cancer TMAs and corresponding healthy tissue were sectioned at a 5-μm thickness for imaging mass cytometry. Sections were de-waxed and rehydrated as described above. Heat-induced epitope retrieval was conducted in a water bath at 88 °C in Tris-EDTA buffer at pH 9 for 20 min. After immediate cooling, the TMA was blocked with 1% BSA in PBS/0.1% Triton X-100 for 30 min. For staining, TMA samples were incubated overnight at 4 °C with an antibody master mix (**Supplementary Tables 1, 5 and 6**). Samples were then washed five times with PBS/0.1% Triton X-100. For the TMA core no. 210 shown in **Figures 2b** and **3** and **Supplementary Figure 5**, the following protocol was used: heat-induced epitope retrieval at 92–94 °C in Tris-EDTA buffer at pH 9 for 20 min. After immediate cooling, the TMA section was blocked with 3% BSA in TBS/0.1% Triton X-100 for 45 min. TMA samples were incubated overnight at 4 °C with an antibody master mix (**Supplementary Table 2**) containing all antibodies except for anti-pSHP2, anti-CD31, anti-TWIST, anti-CD3, anti-SLUG, and anti-EGFR. After a wash step with 2× TBS/0.1% Triton X-100 and 2× TBS, those antibodies were added, and samples were incubated 2.5 h at room temperature and then 1 h at 4 °C. After being washed, samples were dried at room temperature before imaging mass cytometry.

**IFM analysis of adherent cell line.** Cell samples were cross-linked with 4% paraformaldehyde for 20 min and permeabilized using 0.1% Triton X-100 for 3 min, at room temperature. After a 30-min blocking step with 0.5% BSA in PBS, cell samples were incubated with the primary antibodies for 1.5 h and subsequently incubated for 1 h at room temperature with appropriate fluorophore-conjugated secondary antibodies (Alexa Fluor 488 and Alexa Fluor 647). Metal-labeled antibodies were diluted in buffer containing 1% BSA and 0.3% Triton X-100 in PBS (**Supplementary Table 3**). Samples were imaged with a Zeiss Axio Observer.Z1 (camera,



AxioCam MRm; objective, Ec Plan-Neofluar 40× / 0.75 Ph2; filter sets, 02 (DAPI), 38 (Alexa Fluor 488) and 50 (Alexa Fluor 647)). Images were acquired using AxioVision software (AxioVision Rel 4.8), and the acquisition was performed on the same day to prevent differences due to emission changes of the light sources. In addition, exposure times for a given marker were kept constant for the comparative analysis of each antibody. Images were processed using ImageJ software (ImageJ 1.440). Identical settings were applied for processing images of mock and vanadate-treated samples for a given molecular marker (**Fig. 4** and **Supplementary Fig. 7**). Settings were defined by minimum and maximum values modified using a brightness/contrast tool.

**High-spatial resolution laser ablation.** Tissue sections were analyzed by imaging mass cytometry, which couples laser ablation techniques and CyTOF mass spectrometry<sup>23</sup>. A modified ArF excimer GeoLas C laser system (Coherent) delivered a homogenized UV laser beam ( $\lambda = 193$  nm) to an aperture of 25  $\mu\text{m}$ , which was imaged by 25-fold demagnification on the tissue samples. The resulting laser beam of 1  $\mu\text{m}$  in diameter and 3.5 J/cm<sup>2</sup> laser fluence was used to ablate the antibody-stained tissue at a frequency of 20 Hz. The resulting laser ablation crater of the tissue was ~1  $\mu\text{m}$  in diameter (as determined by scanning electron microscopy)<sup>31</sup>. The translation speed of the laser ablation chamber was 20  $\mu\text{m/s}$ . Individual line scans with 1- $\mu\text{m}$  distance were rastered in order to fully remove the tissue layer within the region of interest. The laser ablation chamber used to enable high-spatial resolution, high-sensitivity imaging on the laser ablation system is described in detail by Wang *et al.*<sup>31</sup>. The ablated sample aerosol was directly transported to the CyTOF mass cytometer (Fluidigm (formerly DVS Sciences)) by argon and helium gas flows. The CyTOF instrument settings were described previously<sup>27,30</sup>. The CyTOF software version used was 5.1.598.

**Data analysis and image visualization.** All data processing was performed using in-house-developed Matlab routines (Matlab R2012a). The transient signal data were exported from the mass cytometer in text format. The file consists of push numbers (i.e., time) in rows and mass channels in columns, and the measured values are given as ion counts. The recorded signals in each channel were integrated over 768 pushes, equivalent to a 10-ms time window (1 push  $\approx$  13  $\mu\text{s}$ ). Subsequently, each laser-generated pulse (50-ms duration) in the transient signals was integrated into a single laser shot signal. Finally, images of each mass channel were reconstructed by plotting the laser shot signals in the same order they were recorded, line scan by line scan. For further data analysis, the mean background determined over a duration of ~1 s of each individual channel obtained before the first line scan started was subtracted from each individual image data set (**Supplementary Software**).

**Calculation of the limit of detection.** The limit of detection (LOD) was calculated for signals in a time duration identical to the integration time for a single laser shot (50 ms or one image pixel). The averaged background signals of most of the channels was less than one count per laser shot. On the basis of Poisson statistics, the LOD in ion counts was then determined according to the following formula<sup>41</sup>:  $\text{LOD} = 3.29 \times S + 2.71$ , where  $S$  is the s.d. of the background signal integrated in this time duration

( $S$  is assumed to be square root of the mean background; hence, conservatively estimated,  $S \approx 1$ ). Therefore, the LOD of the image (mean background corrected) was estimated to be six counts per image pixel.

**Single-cell segmentation.** Topological single-cell segmentation is necessary before single-cell protein expression analysis. To detect the cell boundaries in the images, we incorporated the cell membrane proteins  $\beta$ -catenin, HER2 and cytokeratin 8/18 into the experimental protocol; staining for the protein H3 was used to identify cell nuclei. Images showed well-aligned morphological cell boundaries and centers. Further cell segmentation was achieved by watershed transformation<sup>42,43</sup>. First, the membrane images and the negative nucleus image were overlaid to yield maximum cell-boundary information. Then the images were Gaussian blurred to minimize imaging artifacts and noise. Finally, watersheds were searched along the cell membranes with the Matlab imaging toolbox (Matlab R2011b). The best segmentation results were achieved with prior Gaussian blurring (kernel width of 3–4.5 pixels) and standard parameters for watersheds<sup>42</sup>. All single-cell boundaries were visually evaluated and corrected if necessary. The contents of the boundary masks were then subjected to single-cell analysis. All these steps were performed by an in-house-developed Matlab script. Finally, single-cell marker expressions were normalized to the median H3 signal obtained from each image.

**Comparison of single-cell marker intensities.** For immunofluorescence images, the single-cell segmentation was performed using an in-house-developed CellProfiler<sup>44</sup> segmentation pipeline. All intensities were rescaled from 0 to 1, and outliers (<0.1% sample size) were removed. For imaging mass cytometry data, the cell events extracted from the watershed algorithm were analyzed (see above). Preprocessing and further analysis were performed in Matlab 2013a using the Wilcoxon rank-sum test as an alternative to the Student's  $t$ -test, as normal distribution cannot be assumed. The positive and negative single cells were estimated by a globally defined threshold for each method. For each comparison one biological replicate was available.

**SPADE analysis of analyzed tumors.** The cell events extracted from the watershed algorithm were analyzed on <http://cytobank.org/> and using the software tool SPADE<sup>36</sup>. The following summarizes the SPADE algorithm within the context of this imaging-based single-cell analysis. First, density-dependent downsampling of all extracted cell events to a prespecified target number was performed. The following settings were implemented: Arcsinh Cofactor = 5, target number of clusters = 150, downsample to target number of events = 5. The analysis was run by using the software Cytoscape\_v.2.8.3. The downsampled cell events were then clustered according to the expression of 19 markers (ER, PR, CD68, CD20, c-MYC, HER2, pAMPK, H3, pERK, pBad, CD44,  $\beta$ -catenin, vimentin, cytokeratin 7, CAH IX, E-cadherin, pS6, caspase 3 and cytokeratin 8/18) into phenotypically similar agglomerates of cells. Phenotypically similar agglomerates of cells were connected via edges to draw a minimum spanning tree. Next an upsampling step was performed to assign each cell event from the initial data set to the most representative agglomerate. Finally, the minimum spanning tree was projected in two dimensions,





and circles of the tree representing cell agglomerates were colored by median intensity level of a given measured parameter allowing visualization of marker expression across the entire cellular hierarchy. For the SPADE trees representing the cell populations, the node size was given as percent total (for example, number of cells from a given image falling into a cell cluster). Attribute values used are: 0/5/7/15/maximum, node size: 60/120/150/200/200. In **Figure 5**, for HER2, the color bar was set in the range 4–9 with steps 4/4.5/5/6/7/8.5/9. CD20-positive cell subpopulations are displayed, and the color bar was set in the range 0–9 in the following steps: 1/3/5/6/7/8/9. In **Supplementary Figure 11**, the CAH IX-positive cell subpopulations are displayed, and the color bar was set in the range 3.5–8 in the following steps: 3.5/4/4.5/5/5.5/6.5/7.

**Visualization of images.** For visualization only, the images of each individual channel were upsampled to a width of 1,500 pixels, with the image ratio maintained using bicubic automatic resampling in Adobe Photoshop v.13. For image artifact correction, noise reduction was implemented in Adobe Photoshop v.13 with these settings: strength 5, preserve details 2%, reduce color noise 0% and sharpen details 40%. For PR (case nos. 23 and 210) and cleaved caspase 3 (case no. 210), “despeckle” and Gaussian blur (kernel width, 0.25 pixels) before upsampling were applied. For all data analysis steps, only raw data were used unless otherwise mentioned. For **Figure 2b** the scale maximum indicating the

counts per laser shot was adjusted for imaging mass cytometry as followed, from top to bottom: H3, 200; HER2, 30 and H3, 200; CK8/18, 80 and H3, 200; E-cadherin, 40 and H3, 400; vimentin, 80 and H3, 400. For **Figure 3** the scale maximum indicating the counts per laser shot were adjusted as follows. Tissue no. 210: H3, 200; CK8/18, 80; vimentin, 400; CK7, 25; CD44, 50; PR, 10; pan-actin, 40; CD68, 20. Tissue no. 23: HER2, 50; H3, 400; vimentin, 100; E-cadherin, 30; cytokeratin 7, 25; pS6, 20;  $\beta$ -catenin, 40; ER, 40; and CD68, 10. For **Figure 4** the maximum ion counts shown for each protein phosphorylation site were identical between treatment and control conditions, and the scale maximum indicating the counts per laser shot were adjusted as follows: PLC $\gamma$ 2, 600; ERK, 100; p38, 60 and S6, 60.

39. Theurillat, J.P. *et al.* NY-BR-1 protein expression in breast carcinoma: a mammary gland differentiation antigen as target for cancer immunotherapy. *Cancer Immunol. Immunother.* **56**, 1723–1731 (2007).
40. Blurry, R.W. *Immunocytochemistry, a Practical Guide for Biomedical Research* (Springer, 2010).
41. Currie, L.A. Nomenclature in evaluation of analytical methods including detection and quantification capabilities (IUPAC recommendations 1995). *Pure Appl. Chem.* **67**, 1699–1723 (1995).
42. Meyer, F. Topographic distance and watershed lines. *Signal Processing* **38**, 113–125 (1994).
43. Shapiro, L.G. & Stockman, G.C. *Computer Vision* (Prentice Hall, 2001).
44. Kametsky, L. *et al.* Improved structure, function and compatibility for CellProfiler: modular high-throughput image analysis software. *Bioinformatics* **27**, 1179–1180 (2011).